NANO · MICRO small
www.small-journal.com

Dielectric Environment Sensitivity of Carbon Centers in Hexagonal Boron Nitride

Danis I. Badrtdinov, Carlos Rodriguez-Fernandez, Magdalena Grzeszczyk, Zhizhan Qiu, Kristina Vaklinova, Pengru Huang, Alexander Hampel, Kenji Watanabe, Takashi Taniguchi, Lu Jiong, Marek Potemski, Cyrus E. Dreyer, Maciej Koperski, and Malte Rösner**

A key advantage of utilizing van-der-Waals (vdW) materials as defect-hosting platforms for quantum applications is the controllable proximity of the defect to the surface or the substrate allowing for improved light extraction, enhanced coupling with photonic elements, or more sensitive metrology. However, this aspect results in a significant challenge for defect identification and characterization, as the defect's properties depend on the the atomic environment. This study explores how the environment can influence the properties of carbon impurity centers in hexagonal boron nitride (hBN). It compares the optical and electronic properties of such defects between bulk-like and few-layer films, showing alteration of the zero-phonon line energies and their phonon sidebands, and enhancements of inhomogeneous broadenings. To disentangle the mechanisms responsible for these changes, including the atomic structure, electronic wavefunctions, and dielectric screening, it combines ab initio calculations with a quantum-embedding approach. By studying various carbon-based defects embedded in monolayer and bulk hBN, it demonstrates that the dominant effect of the change in the environment is the screening of density–density Coulomb interactions between the defect orbitals. The comparative analysis of experimental and theoretical findings paves the way for improved identification of defects in low-dimensional materials and the development of atomic scale sensors for dielectric environments.

1. Introduction

Point defects in semiconductors and insulators have emerged as robust and manipulatable quantum systems for applications such as qubits for quantum computers,[1–4] single-photon emitters (SPEs) for quantum communication,[5,6] and nanoprobes for quantum metrology.[7] In this context, 2D vdW bonded compounds have been proposed as promising host materials. One key benefit arises from the potentially atomically perfect surfaces of these materials. Quantum defects may reside in close proximity to the surface without suffering instabilities in their optoelectronic and/or coherence properties due to surface dangling bonds, adsorbates, or local charge variations. This has several advantages for creating sensors of local fields at the nanoscale, better extraction efficiency for defect SPEs, and direct imaging or manipulating defects by scanning probe techniques.[8,9] The most developed of such host material is hexagonal boron nitride (hBN).[10,11] It is widely available[12] and its large bandgap is

D. I. Badrtdinov, M. Rösner
Institute for Molecules and Materials
Radboud University
Heijendaalseweg 135, 6525 AJ Nijmegen, Netherlands
E-mail: m.roesner@science.ru.nl

C. Rodriguez-Fernandez
Faculty of Engineering and Natural Sciences
Tampere University
Tampere 33720, Finland

M. Grzeszczyk, K. Vaklinova, P. Huang, M. Koperski
Institute for Functional Intelligent Materials
National University of Singapore
Singapore 117544
E-mail: msemaci@nus.edu.sg

The ORCID identification number(s) for the author(s) of this article can be found under https://doi.org/10.1002/smll.202300144

DOI: 10.1002/smll.202300144

Z. Qiu, L. Jiong
Department of Chemistry
National University of Singapore
117543, Singapore

P. Huang, M. Koperski
Department of Materials Science and Engineering
National University of Singapore
Singapore 117575, Singapore

P. Huang
Guangxi Key Laboratory of Information Materials
Guilin University of Electronic Technology
Guilin 541004, China

A. Hampel, C. E. Dreyer
Center for Computational Quantum Physics
Flatiron Institute
162 5 th Avenue, New York NY 10010, USA

conducive to the formation of deep quantum levels. There have been many reports indicating hBN hosts SPEs[13–16] with some allowing for spin manipulations.[17–19] Specifically, it has been shown experimentally[20–25] and theoretically[26–37] that carbon impurities in hBN can give rise to a plethora of defect centers with a wide variety of properties attractive for quantum applications.

The existence of defects in proximity to surfaces and interfaces also presents a significant challenge. Quantum technologies often require arrays of defects with identical properties and though the surfaces and interfaces of the substrate can be atomically clean, proximity to them may change the properties of the defect, including emission energies and linewidths.[38] For example, hBN films are usually multilayer and range from tens of nanometers to a few atomic layers. Even a defect with the same chemical composition may exhibit different experimental signatures depending on its position with respect to the interface, surface, or edge of the film. A quantitative understanding of these effects is necessary for defect identification and quantum applications.

In order to understand the influence of surfaces and interfaces on the properties of defects in hBN and other 2DvdW materials, several effects must be disentangled. First, the different distances to surrounding atoms or vacant spaces may change the structure of the defect, especially if it involves displacements of atoms out of the 2D plane. Such structural modifications will also impact the electron-lattice coupling responsible for the phonon broadening of optical transitions. The electronic wave functions associated with the defect states may also evolve according to the variations in symmetry and environment. Additionally, the alteration of the dielectric screening environment experienced by the defect will modify the Coulomb interactions between electrons occupying the defect levels. The latter has been recognized before as an important contribution to correlation effects in layered materials, such as for exciton formation[39–41] and magnetism.[42] The relative importance of all of these factors is expected to differ between defects with different atomic and electronic structures of the ground and excited states.

In this study, we use a combination of experimental characterization (optical and scanning probe spectroscopy) and first-principle theoretical analysis to elucidate how the surroundings of defects in hBN influence their properties. Experimentally, we inspect this via studying the sensitivity of optical defect properties to the thickness of the hBN samples. This is enabled by intentional carbon doping, which allows us to create reproducible defect centrers with stable photoluminescence (PL) resonances. Thus, we can control the defect density and the proximity of the defects to the surface by isolating hBN films of varied thicknesses. We demonstrate the evolution of the optical spectra from ensembles of specific defect types in ≈50 nm thick hBN films to individual defects in ≈10 atomic layers of hBN. We interpret the modification of the PL spectra based on a combination of density-functional theory (DFT) calculations and a recently-developed quantum embedding approach.[33] Using the experimental characterization as a guide to the types of defects to analyze, we consider theoretically the two extremes in defect surroundings: defects in a free-standing monolayer of hBN, and defects in infinite bulk hBN. We calculate the changes to the atomic and electronic structure of the defects relevant to, e.g., the optical measurements.

We find that the dominant effect of the environment is the change in dielectric screening, which affects the intra- and interorbital density–density Coulomb interaction between electrons in defect states. The enhanced screening in the bulk form of the crystal significantly reduces the energy of intradefect optical transitions if they depend on such interactions. Based on this, we propose that this sensitivity to the dielectric environment can be utilized as a sensor for local dielectric constants when brought into contact with surfaces, adsorbates, or liquids. We find that the optical transitions within the substitutional carbon dimer have the potential for such applications.

The paper is organized as follows. In Section 2 we summarize our optical and scanning-probe measurements, which serves as the experimental motivation for the systematic theoretical study of environmental effects on defects given in Section 3. In Section 4 we discuss the main results and the implications for defect identification/characterization, as well as the use of defects to detect changes in a dielectric environment.

2. Experimental Results: Characterization of Carbon-Enriched hBN

We characterize ultra-pure hBN crystals grown via high-pressure-temperature gradient methods. Carbon doping is achieved post-growth by annealing the crystals in a graphite furnace at 2000 °C for one hour, which gives rise to multiple optically active defect centres[24] in few-layer and bulk hBN. Details on the growth and sample fabrication are given in the Methods section.

K. Watanabe
Research Center for Functional Materials
National Institute for Materials Science
Tsukuba 305-0044, Japan

T. Taniguchi
International Center for Materials Nanoarchitectonics
National Institute for Materials Science
Tsukuba 305-0044, Japan

L. Jiong
Centre for Advanced 2D Materials
National University of Singapore
Singapore 117546, Singapore

M. Potemski
Laboratoire National des Champs Magnétiques Intenses
CNRS-UGA-UPS-INSA-EMFL
25 Av. des Martyrs, 38042 Grenoble, France

M. Potemski
CENTERA Labs
Institute of High Pressure Physics
PAS PL-01-142, Warsaw Poland

M. Potemski
Faculty of Physics
University of Warsaw
ul. Pasteura 5, 02-093 Warszawa, Poland

C. E. Dreyer
Department of Physics and Astronomy
Stony Brook University
Stony Brook, New York 11794-3800, USA

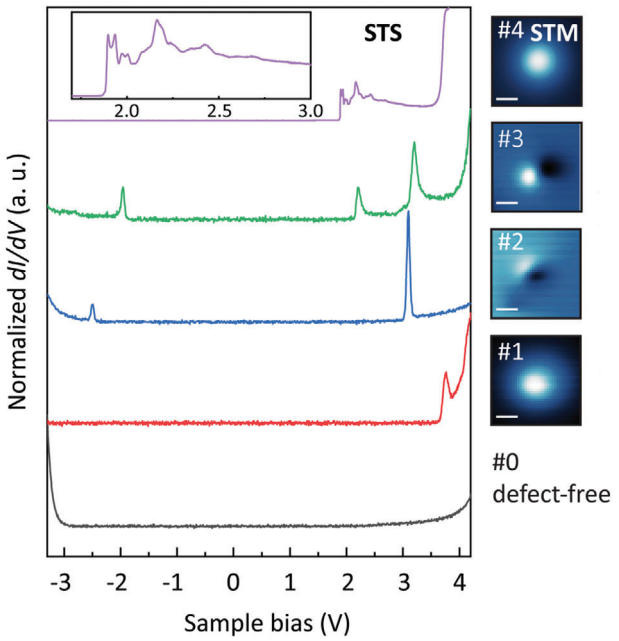

Figure 1. STS spectra for defects located in three-layer thick carbon-doped hBN film, which were initially identified through STM. The STM images are presented next to the corresponding STS curves. All experiments were performed at the temperature $T = 77$ K, except for the defect #4, which was inspected at $T = 4.7$ K. STM images of defects #1–#3 were measured under the conditions $V_s = 5{\sim}V$, $I_t = 30{\sim}pA$. For defect #4, STM image was obtained under the conditions $V_s = 4.5{\sim}V$, $I_t = 100{\sim}pA$. The STS #0 was measured on a pristine hBN area free of defects. The inset constitutes the magnified image of the STS curve of defect #4, which demonstrates the fine structure of the vibronic response arising due to the electron-phonon coupling. The scale bar in the STM images corresponds to 2 nm.

With these experimental characterizations we aim to a) determine the general properties of carbon defects in hBN hosts, b) motivate the choices of defects for our theoretical study, and c) inspect how the local impurity environment controlled by the host thickness changes the defect properties.

In **Figure 1** we depict representative scanning-tunneling microscopy/spectroscopy (STM/STS) measurements on a three-layer-thick hBN sample exemplifying the huge variety of carbon-related defects that may occur in hBN.[27,35–37] The STM data (panels on the right) demonstrates well-isolated defect centers that appear as symmetric or asymmetric features in the color maps. In the dI/dV STS spectra we see that several of these defects (labelled #1 to #3), involve resonances near the hBN conduction or valence bands, consistent with simple defects, such as carbon substitutions for boron or nitrogen vacancies.[23,26,32] Accordingly, we start with simple defects in our theoretical modelling discussed in Section 3.

In **Figure 2** we present PL and second-order photon correlation data for carbon enriched bulk-like (ca. 50 nm) and thin-film (about 10 layers) hBN hosts. In Figure 2a, we show the PL spectrum together with a comparative analysis of the four most pronounced defect centers given in Figure 2b–e in the bulk-like hBN host. Defect A1 displays emission in form of a broad asymmetric band indicative of strong electron-phonon coupling. The emission spectra of defects A2 and A4 are dominated by narrow resonances characteristic of centres exhibiting atomic

Table 1. Experimentally measured Debye-Waller and Huang-Rhys factors of defects A1-A4 responsible for the luminescence peaks in Figure 2a.

Defect	ZPL	Debye-Waller factor	Huang-Rhys factor
A1	1.38 eV	$\leq 0.032 \pm 0.006$	$\geq 3.4 \pm 0.2$
A2	1.54 eV	0.29 ± 0.08	1.2 ± 0.3
A3	2.00 eV	0.12 ± 0.03	2.1 ± 0.2
A4	2.31 eV	1.0	≈ 0.0 (atomic)

character.[24] Defect A3 displays a spectrum typically observed for more complex defect structures such as nitrogen-vacancy centers in diamond, where the well-pronounced dominant zero-phonon line (ZPL) is accompanied by lower-energy phonon sidebands.[24]

We can characterize the luminescence signatures of the bulk hBN defect centers in the framework of a simple 1D Franck-Condon model.[43] In that model, the lineshape is governed by the coupling of the electronic transition to a single effective vibrational mode and is parameterized by the Huang-Rhys factor S_{HR}, which gives the average number of phonons emitted in an optical transition. S_{HR} depends on the difference in atomic structure between the electronic states involved in the transition, and the curvature of the potential energy surface for each state with respect to displacements of the effective vibrational mode. Experimentally, S_{HR} can be determined from the ratio of the spectrally integrated intensity of the ZPL and the intensity of the total defect emission (i.e., the Debeye-Waller factor $w = I_{ZPL}/I_{total}$) using the phenomenological relation $S_{HR} = -\ln(w)$. In **Table 1** we present w and S_{HR} for the defects in bulk-like hBN. We see that they are characterized by small to medium strength of the electron-phonon coupling. For A1, the value of S_{HR} should be taken as a lower bound since the ZPL is not discernible. Similarly, the phonon sideband for A4 is not distinctive, and thus we report S_{HR} near zero.

Since these defect centers yield reproducible and well-recognizable spectral characteristics, we can directly compare defects in the bulk-like and few-layer samples. In Figure 2f,g we show the corresponding PL spectra for energies around A3 and A4 in bulk and ten-layer thick hBN:C films (see Supplemental Information for further examples). Importantly, we find for both hBN thicknesses PL resonances at similar but not identical emission energies. In the A3 energy range, we see that the ZPL blueshifts by about 50 meV from the bulk to the ten-layer sample, which is accompanied by a reduction of the ZPL linewidth (reduction of I_{ZPL}) indicative of the removal of inhomogeneous broadening and by an increasing Huang-Rhys factor S_{HR} from 2.1 to 3.2. As the phonon sideband is not drastically affected, we attribute the enhanced S_{HR} to the reduced inhomogeneous ZPL broadening.

The two-peak structure of A4 is visible for both hBN thicknesses and shows a linewidth reduction, without clear signs of a blueshift and the same value of $S_{HR} \simeq 0$. For both defect types, in the few-layer sample, we confirm that we are probing individual defects[15,44,45] by measuring the antibunching in the second order correlation function $g^{(2)}(\tau)$ [see Figure 2h,i].

These optical measurements explicitly reveal the significant changes in defect properties, but the particulars vary from defect to defect. This observation provides the motivation for our

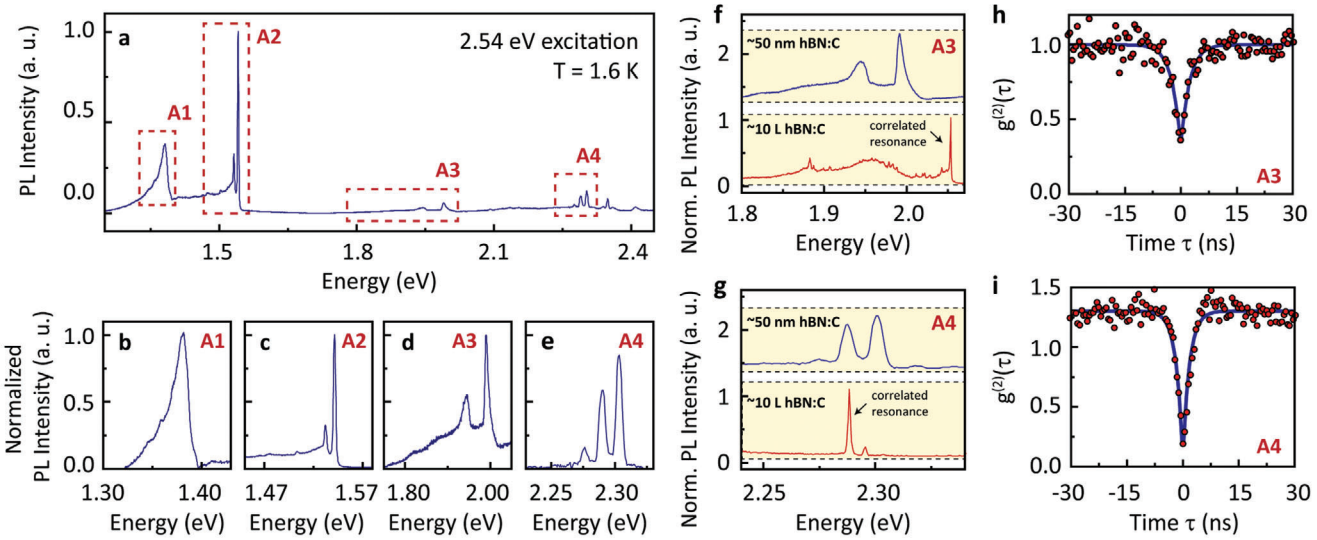

Figure 2. The PL spectra of bulk (about 50 nm thick) hBN:C film measured at low temperature (1.6 K) in microscopic backscattering geometry (a). Four distinct spectral features can be identified, which we attribute to specific defect centres active in near-infrared (A1 and A2) and visible (A3 and A4) spectral regions. The spectra of the specific defects (b–e) are normalized toward uniform maximum intensity for ease of comparison. A comparative representation of PL spectra of hBN:C in the bulk limit (≈50 nm thick) and a few layers' limit (about ten layers) is presented for defects A3 (f) and A4 (g). The second-order photon correlations $g^{(2)}(\tau)$ measurements done for the emission resonances in ten-layer thick films demonstrate an antibunching indicative of single photon emission for defects A3 (h) and A4 (i).

theoretical investigation of environmental effects on different defects in the next section. Since the attribution of such optical signals with specific defects is still controversial, we will discuss general defects that are likely to exist in hBN:C samples,[27,35–37] and provide further commentary on how our results could be used to aid defect identification in Section 4.

3. Theoretical Modelling Results

We now analyze theoretically how changes to the structural and screening environment caused by different hBN host thicknesses affect intradefect excitations and their associated Huang-Rhys factors. We consider a variety of charge-neutral native and C-containing defects in three different situations: bulk ($P6_3/mmc$), "constrained" monolayer, and free-standing monolayer hBN, as depicted in **Figure 3**. The bulk and monolayer structures are fully relaxed, while the constrained monolayer structure is taken from the bulk structure without any further lattice relaxations. With these three structures, we are able to theoretically disentangle the effects of screening and atomic relaxations going from bulk to monolayer hBN hosts. We note that well-controlled impurities in free-standing monolayer hBN are difficult to realize in realistic samples; nevertheless, the monolayer hosts serve as a theoretical limit with the strongest environmental impact to the defect centers. We combine first-principles DFT calculations with the quantum embedding scheme described in Ref. [33], which allows us to systematically study how changes in the environment and modifications in the impurity structure in the ground and excited states affect the impurity properties.

3.1. Computational Approach

For each of the cases depicted in Figure 3, the atomic relaxations around the defect is treated at the DFT level, and constrained DFT calculations are used to relax the defect structure in excited electronic states. We furthermore estimate how the electron-phonon coupling associated with defect transitions is affected in each case

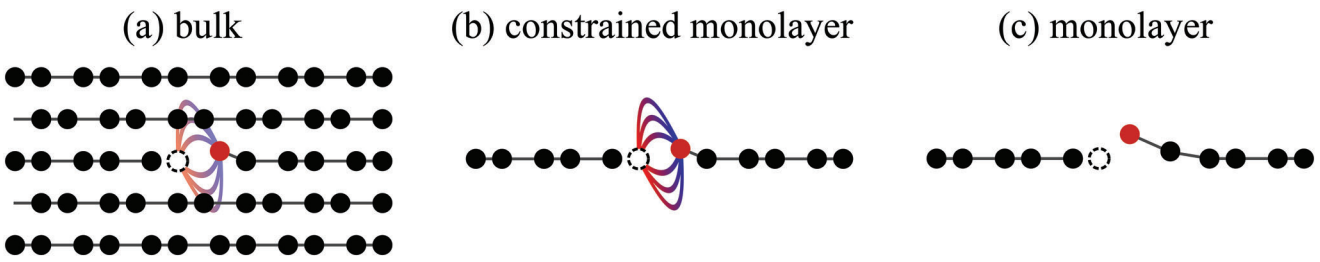

Figure 3. Schematic of theoretical situations used to isolate different environmental effects to impurity complexes (vacancies and C substitutions, the latter in red) embedded in 2DvdW hBN hosts (black). a) Bulk: defect in the infinite bulk environment. b) Constrained monolayer: defect in a monolayer constrained to the monolayer structure as in the bulk case. c) Monolayer: defect with fully relaxed structure in monolayer. In (a) and (b) we sketch intradefect electric field lines to highlight the difference in the screening environment. Note in (c) that the impurity positions are different.

by evaluating the Huang-Rhys factor S_{HR}, introduced in the previous section. A full picture of the vibrational coupling requires determining S_{HR} for all relevant modes in the system, which is a challenging task for transitions with moderate $S_{HR} \approx 3$ as the defects observed in PL;[46,47] however, often a qualitative picture of the strength of the electron-phonon coupling can be obtained by considering a single effective mode corresponding to the structural difference between the ground and excited electronic states.[48,49] Under this assumption, and presuming the vibrational coupling is equal in the excited and ground state, $S_{HR} = E_{FC}/\hbar\omega$, where $E_{FC} = (E_{abs} - E_{em})/2$ is the Frank-Condon relaxation energy (i.e., half of the difference between vertical absorption and emission energies), and ω is the frequency of the mode.[43,48,50] In addition, if we assume that the mode is harmonic, we can write $S_{HR} = \frac{\Delta Q}{\hbar}\sqrt{\frac{E_{FC}}{2}}$, where ΔQ is the absolute change of the nuclear coordinate between the ground and excited defect state indicative of the renormalization of the inter-atomic bond strength.

The impact of changing the defect environment from monolayer to bulk hBN to the electronic properties of the defects will be elucidated using an embedding approach within which we map the complicated many-electron problem of the defect in hBN to an effective minimal Hamiltonian with only a small number of defect-related states i, j, k, l of the form:

$$H = -\sum_{ij,\sigma}(t_{ij}c^{\dagger}_{i\sigma}c_{j\sigma} + \text{H.c.}) + \frac{1}{2}\sum_{ijkl,\sigma\sigma'}U_{ijkl}c^{\dagger}_{i\sigma}c^{\dagger}_{j\sigma'}c_{l\sigma'}c_{k\sigma} - H_{DC} - \mu\sum_{i,\sigma}c^{\dagger}_{i\sigma}c_{i\sigma} \quad (1)$$

where μ is the chemical potential to control the occupation of the defect states, σ is the spin, and $c^{\dagger}_i$ and c_i are corresponding electronic creation and annihilation operators. H_{DC} denotes the so-called double counting correction term.[33] Diagonalizing this Hamiltonian results in many-body energies and wavefunctions of intradefect excitations.

The "active space" of defect-related states is isolated from the host hBN electronic structure via the construction of Wannier functions, which allows us to determine the hopping matrix elements t_{ij}. Changes in the hopping matrix elements reflect changes in the properties of the defect states on the DFT level. The screened Coulomb matrix elements U_{ijkl} are computed in the static constrained random-phase approximation (cRPA),[51] which takes the environmental screening into account. Comparing the *unscreened* (bare) Coulomb matrix elements v_{ijkl} (which are only sensitive to changes in defect Wannier functions) with U_{ijkl} gives us insight into how the dielectric environment changes from bulk to monolayer hBN hosts and how this affects the intradefect transition energies. For computational details, see the Methods section.

We can also obtain E_{FC} from the intradefect transitions calculated from the many-body energies of Equation (1). To this end, we calculate the transition energy in both the ground state geometry and the excited state geometry. Under the assumptions discussed above, half of their difference gives E_{FC}.

Table 2. Bare ($v = v_{iiii}$) and screened ($U = U_{iiii}$) Coulomb matrix elements (in eV) of single C impurities. $\epsilon = v/U$ is the effective dielectric constant.

	monolayer			bulk		
	v	U	ϵ	v	U	ϵ
C_B	6.27	2.65	2.4	6.54	1.70	3.9
C_N	7.25	2.85	2.5	7.04	1.87	3.8

3.2. Single Carbon Impurities

We start our theoretical discussion with single carbon impurities either replacing a boron (C_B) or a nitrogen (C_N) site, as depicted in **Figure 4**. Both yield single occupied in-gap states, close to the hBN conduction band (C_B) or valence bands (C_N), in good qualitative agreement with the STS/STM data shown in Figure 1 and as previously reported.[22,23]

With only one electron in a single state, there are no intra-impurity excitations possible.[20] Nevertheless, these most simple defects already allow us to study the impact of the environment on the impurity orbitals. For both of these cases, the change in atomic structure between bulk and monolayer is negligible, with C-N (C-B) bond lengths changing by only 0.003 Å (0.004 Å) in good agreement with previous data on the difference between mono- and bilayer hosts.[31]

We construct localized Wannier orbitals for both C impurities, as depicted in Figure 4b. These p_z-like Wannier functions allow us to calculate the on-site energies t_{ii}, bare ($v = v_{iiii}$) and cRPA screened ($U = U_{iiii}$) Coulomb matrix elements, which we list in **Table 2**. We see that the difference in the bare Coulomb matrix elements between monolayer and bulk hBN hosts is quite small ($\approx$4%), indicating that the single-particle electronic structure [i.e., the shape of the p_z-like Wannier functions, see Figure 4b] does not change significantly between monolayer and bulk. However, U changes significantly, increasing by more than 50% in the monolayer case compared to bulk. We can cast this into a change in the effective dielectric constants $\epsilon = v/U$ felt by the electrons in the defect state; for bulk and monolayer hBN we find $\epsilon \approx 3.8$ and $\approx$2.4, respectively. Note that this trend follows the out-of-plane dielectric constant decrease from bulk to monolayer hBN.[52]

3.3. Boron and Nitrogen Vacancies

Boron and nitrogen vacancies, V_B and V_N, have been discussed in the the literature.[53–55] On the DFT level they yield more complex impurity states, as illustrated in Figure 4. The V_N defect gives rise to a half-filled level below the conduction band accompanied by two additional nearly degenerate empty defect levels within the edge of the conduction band, which is also in qualitative agreement with the STS/STM data of impurity #1 in Figure 1a and Ref. [13]. The V_B defect creates three levels originating from the dangling bonds due to the missing B atom. Two of these states are in close vicinity to the valence band edge, nearly degenerate, and host together one electron, while the third level is deeply buried within the valence band.[18] In these cases, the hopping matrix t_{ij} has a 3×3 form, while the screened Coulomb interaction U_{ijkl} is a rank-4 tensor with three elements per dimension. To compare the Coulomb interactions, we define the average

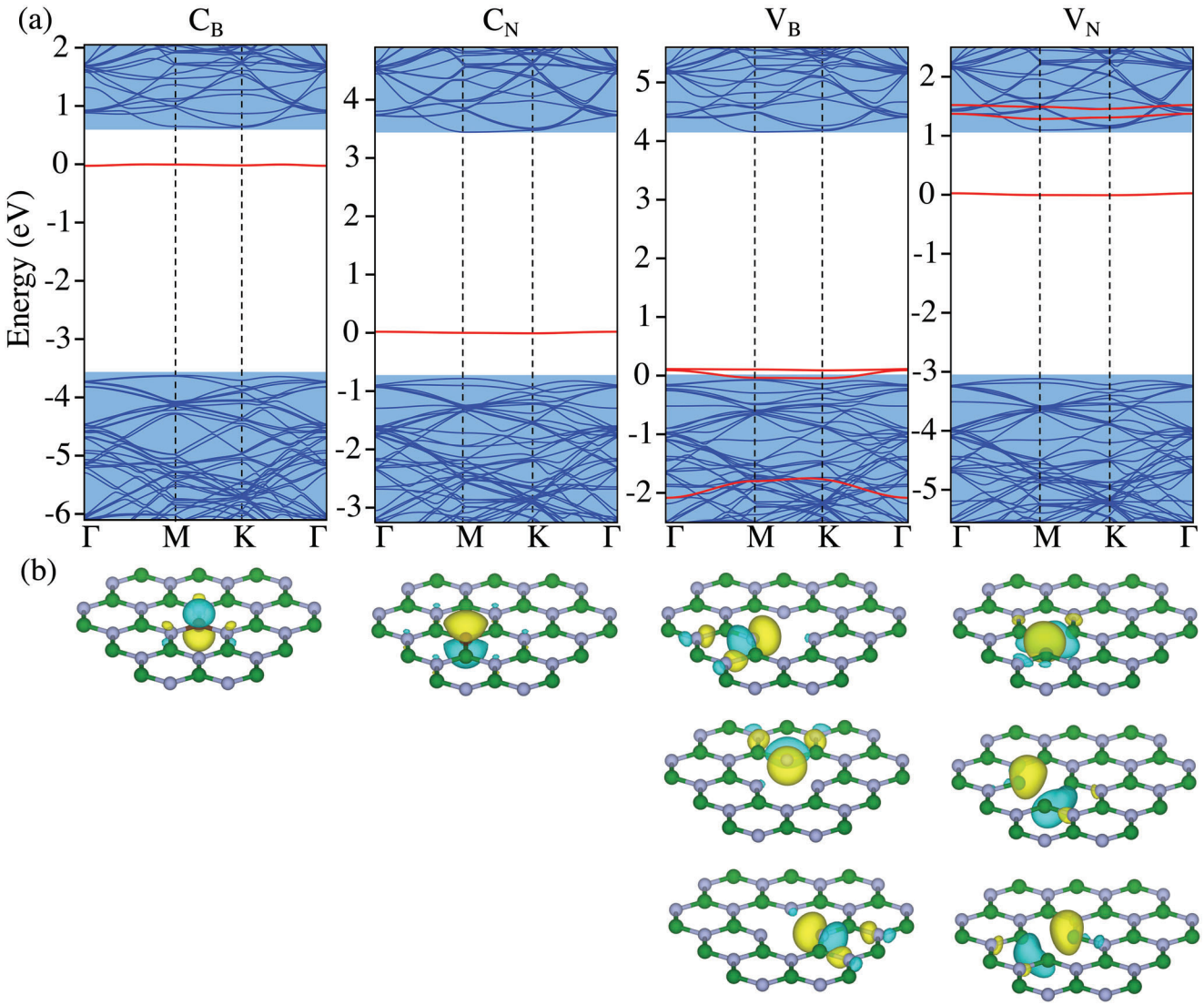

Figure 4. a) DFT band structure of hBN bulk in the presence of carbon substitution centers and vacancies. Defect states are highlighted with red colors and are parametrized using Wannier functions (b).

intra-orbital density-density interaction $U_0 = N_{\text{orb}}^{-1} \sum_i U_{iiii}$, inter-orbital density–density interaction $U_1 = [N_{\text{orb}}(N_{\text{orb}} - 1)]^{-1} \sum_{i \neq j} U_{ijij}$, and exchange interaction $J = [N_{\text{orb}}(N_{\text{orb}} - 1)]^{-1} \sum_{i \neq j} U_{ijji}$, where N_{orb} is the number of Wannier orbitals. Furthermore, we define the effective dielectric constant $\epsilon = \nu_l^{(d)} / U_l^{(d)}$ using the leading eigenvalues of the bare and cRPA screened density–density Coulomb matrices.[56]

In **Table 3** we compare all these parameters together with the single-particle energy separation $\Delta E = t_{00} - t_{11}$ between Kohn-Sham eigenvalues for monolayer and bulk hBN hosts. We find that single-particle energies associated with these defects [and thus the hoppings in Equation (1)] change by 2% for V_B and 4% for V_N. In contrast, the screened density–density interactions decrease significantly from monolayer to bulk hosts by more than 50%. Similar to the screening effects for the C substitutional defects, this is driven by the effective dielectric constants decrease from ≈3 in the bulk to ≈2 in the monolayer. Notably, the exchange elements J are nearly unaffected by the changes in the environment as a result of their dipolar character. Indeed, macroscopic dielectric environmental screening mostly affects density–density Coulomb interactions in layered materials and does not significantly affect non-density-density elements.[42,56] Thus, many-body properties which are

Table 3. Coulomb matrix elements (in eV) of single B/N vacancies. See Section 3.3 for the definition of variables.

	monolayer					bulk				
	U_0	U_1	ϵ	J	ΔE	U_0	U_1	ϵ	J	ΔE
V_B	5.04	2.17	2.4	0.03	1.86	3.45	1.31	3.6	0.03	1.82
V_N	3.50	3.00	2.2	0.23	1.60	2.47	2.00	3.2	0.23	1.54

Table 4. Many-body states of single B/N vacancies.

Impurity	spin	E_n monolayer (in eV)	E_n bulk (in eV)
V_B	Q_0	0	0
	Q_1	0.51	0.63
V	Q_2	2.82	2.31
	D_1	3.18	2.61
	D_2	3.63	3.00
	Q_3	4.63	4.04
V_N	D_0	0	0
	Q_1	1.48	1.37

strongly affected by density–density Coulomb interactions, such as charge excitations, will be in general most prone to changes in the dielectric environment, e.g., resulting from the transition from bulk to monolayer hBN, while exchange interaction driven many-body states, such as spin excitations, will be less affected.

This behavior is visible in the many-body energies of V_B, as summarized in **Table 4**. For both monolayer and bulk hBN hosts, the V_B ground state corresponds to four-times degenerate quadruplet state Q_0, which is approximately given by three electrons fully occupying the lowest and partially occupying the degenerate single-particle states. From the corresponding excitation energies, we find that nearly all excited states decrease in energy by about 500 to 600 meV (with Q_1 as the sole exception) in bulk. This demonstrates that these transitions are decisively affected by the density–density Coulomb interactions.

For V_N we find a similar trend with doublets as the ground state and the following quadruplet excited state. However, all these states are occupied by a single electron, which eliminates any Coulomb contribution. The differences we see in the excited energies stem from the slightly altered single-particle properties as indicated in Table 3.

3.4. Impurity Complexes

The picture that emerges from the simple defects discussed in the previous two sub-sections outlines the key role of differential dielectric screening, which influences density–density Coulomb interactions within and between defect orbitals, inducing a change in the properties upon varying the defect environment from bulk to monolayer hBN.

We now consider more complex defect/impurity structures, which have in-gap intradefect transitions with possible technological relevance, and that could be detected by optical means, as exemplified in the previous section. Specifically, we consider a carbon dimer (C_BC_N)[29,31,33,34] replacing nearest-neighbor B and N atoms with carbon, a carbon-vacancy complex ($C_B V_N$),[28,30,57] and a combination of a dimer with a neighboring vacancy ($C_BC_N V_N$).[37] Especially C_BC_N has recently attracted significant attention, as it was proposed as the origin of the 4.1 eV ZPL single-photon emitter[20,22,58] observed in hBN based on the energetics of emission[29] and calculations of photoluminescence lineshapes.[59,60] All these impurity complexes have modest formation energies[36,37] and are thus likely to occur in both, monolayer and bulk hBN upon C exposure. In **Figure 5** we summarize all model details.

From the DFT band structure calculations presented in Figure 5a–c we see that all three impurity complexes form in-gap defect states with varying occupations (two electrons in C_BC_N and $C_B V_N$ and three electrons in $C_BC_N V_N$). We use these states as the active space for our minimal modelling (see Section S3, Supporting Information for details). The resulting lowest excited many-body levels are shown in Figure 5d–f with indications of the ground and excited state types, singlets (S), doublets (D), triplets (T), and quadruplets (Q). We show these energies calculated for the three cases schematically depicted in Figure 3. Comparing the "constrained monolayer" case to the fully relaxed bulk and monolayer cases allows us to isolate the effects of the dielectric environment from changes in structure from the atomic environment. We thus first comment on the comparison between bulk and "constrained monolayer" hBN hosts, and then on the effect of relaxations between bulk and monolayer hosts.

Throughout all impurity complexes, we see a consistent trend of decreasing optical transition energies when changing from the constrained monolayer to bulk hBN. Upon allowing for further relaxation of the monolayer host system, this trend is mostly preserved. The decreasing excitation energies are more pronounced for singlets than for doublets and are often vanishingly small for triplets and quadruplets, which is a direct measure of how much the many-body states are controlled by density–density and exchange Coulomb matrix elements, as illustrated for each defect below.

3.5. Many-Body States

3.5.1. C_BC_N Many-Body States

The C_BC_N carbon dimer impurity has been widely discussed before, see, e.g., Refs. [29, 31, 34]. It can be approximately modeled as a half-filled Hubbard dimer[33,61] whose many-body eigenstates are solely controlled by the ratio of the local density–density Coulomb repulsion U and the hopping t between the sites. In our case this dimer is formed by localized p_z-like orbitals at the two C positions with local U_0 and interorbital Coulomb interactions U_1, see Figure 5a. In this scenario the effective local Coulomb interaction magnitude is approximately given by $U^* = U_0 - U_1$.[62,63] Upon increasing the screening from monolayer to bulk, both U_0 and U_1 are significantly but similarly reduced (e.g., $\Delta U_0 \approx 1.3$ eV and $\Delta U_1 \approx 1.1$ eV), such that the resulting U^* differ by $\Delta U^* \approx 0.2$ eV. This corresponds to a relative change of nearly 40%. As the electronic hopping between the two p_z Wannier functions is affected by only 3% through the monolayer to bulk transition, we can again state that modifications to the many-body properties are mostly driven by the changes in the dielectric screening. This explains the reduction of the S_1 state by about 0.2 eV and is in agreement with previous GW+BSE and TD-DFT based results.[31,34] In contrast, the lower triplet states T_1 is less affected by this screening, as it depends more strongly on Hund's exchange elements, which are nearly unaffected (see Supporting Information Table SIV). Further, the data presented in Figure 5d

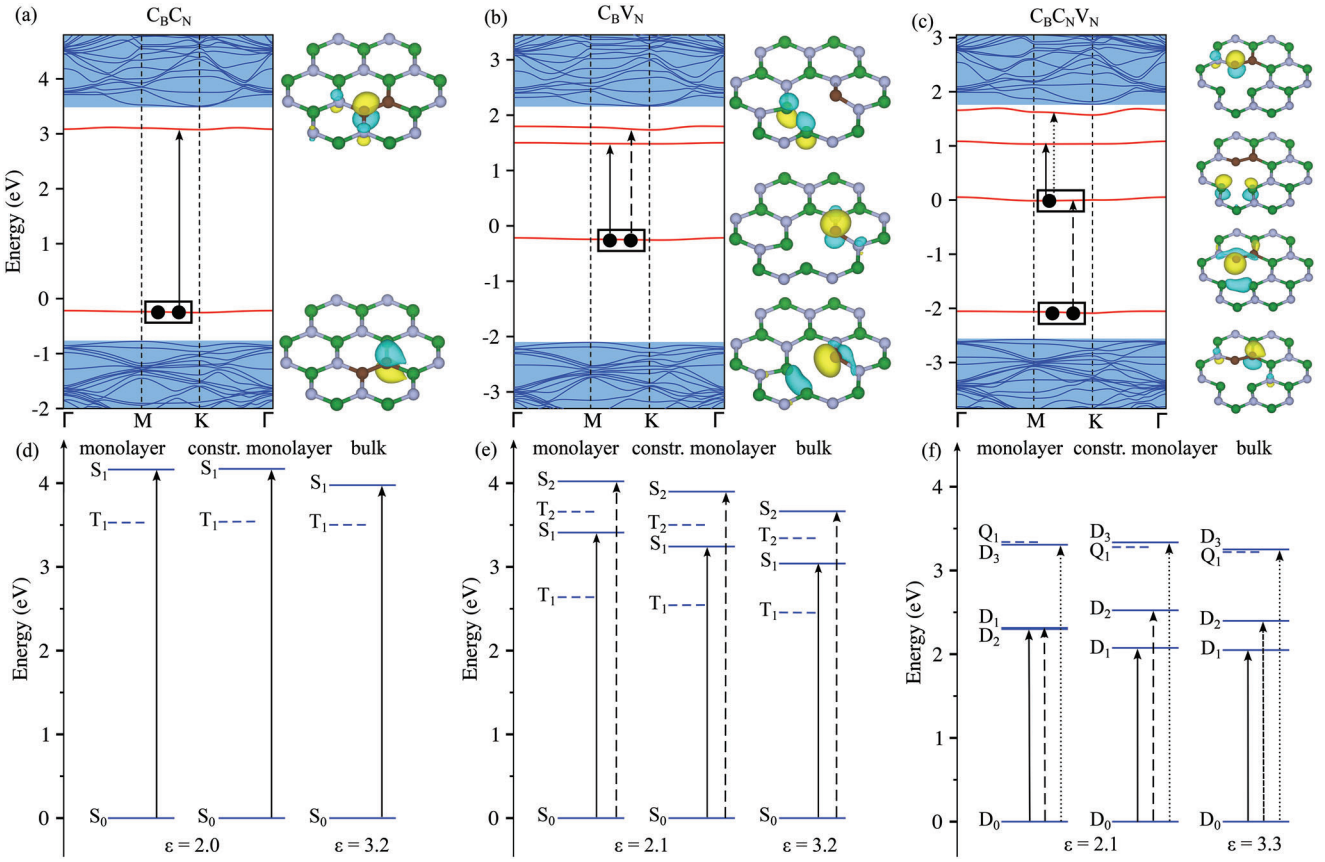

Figure 5. a–c) DFT band structures of each considered impurity complexes embedded into bulk hBN with highlighted in red impurity states, which were parametrized using Wannier functions. Black dots sketch the initial occupations and their modification upon optical excitations. d–f) Many-body impurity states embedded into bulk, constrained monolayer, and free-standing monolayer of hBN. Arrows demonstrate the possible excitations, which properties are given in Table 5.

shows that atomic relaxations of the defect between bulk and monolayer do not play a significant role here (c.f. constrained monolayer and monolayer).

3.5.2. C_BV_N Many-Body States

For C_BV_N the spinless DFT Kohn-Sham (KS) ground state is approximately given by two electrons mostly residing in a C-centered p_x-like state (see side panel of Figure 5b) with a distortion of the C atom position out of the plane.[55] The fully interacting many-body ground state of this impurity can be well approximated as a single Slater determinant with two electrons of opposite spin in the lowest KS state forming a singlet ground state.[28,30,57] The many-body singlet–singlet transitions approximately promote one of these electrons either into a C-centered p_z-like state ($S_0 \rightarrow S_1$, which lets the C atom relax back to the hBN plane)[28,57] or into a delocalized state with two p_z-like wavefunctions centered at the neighboring B atoms ($S_0 \rightarrow S_2$ with reduced out-of-plane C position distortion). The bulk screening reduces the corresponding transition energies by 0.2 eV and by 0.24 eV for S_1 and S_2, respectively (c.f. constrained-monolayer to bulk transitions in Figure 5e). A similar approximate U^* analysis (using orbital averaged U_0 and U_1 given in the Supporting Information) yields an estimate of $\Delta U^* \approx 0.2$ eV (ca. 20%). As the single-particle energies only change by less than 5% and since the Hund's exchange elements are nearly unaffected between the bulk and constrained monolayer hosts, the overall trend in the many-body levels can again be explained based on modifications to the density–density Coulomb matrix elements. Full relaxations toward the free-standing monolayer enhance the out-of-plane C position distortion, which mainly affects the single-particle energies, while screened density–density and Hund's exchange elements are nearly unaffected (see Table SV, Supporting Information). The single-particle KS energies change by about 0.1 to 0.2 eV in the freestanding monolayer with respect to the constrained monolayer, which is the same order of magnitude as the many-body excitation energies change between the two systems.

3.5.3. $C_BC_NV_N$ Many-Body States

This defect complex can be interpreted as a combination of C_BC_N and C_BV_N. The KS ground state corresponds approximately to a fully occupied p_z-like state centered on the C atom farthest from the vacancy and a half occupied p_x-like state centered at the

Table 5. The absolute change of configuration coordinates ΔQ (in $\sqrt{\text{amu}}$ Å), Franck-Condon energy E_{FC} (in eV) and Huang-Rhys factor S_{HR} for impurity complexes embedded into free-standing monolayer and bulk hBN.

	C_BC_N						C_BV_N						$C_BC_NV_N$					
	monolayer			bulk			monolayer			bulk			monolayer			bulk		
#	ΔQ	E_{FC}	S_{HR}	ΔQ	E_{FC}	S_{HR}	ΔQ	E_{FC}	S_{HR}	ΔQ	E_{FC}	S_{HR}	ΔQ	E_{FC}	S_{HR}	ΔQ	E_{FC}	S_{HR}
1	0.24	0.06	0.65	0.26	0.07	0.75	3.37	0.80	33.0	2.00	0.62	17.20	2.95	0.59	24.80	1.68	0.44	12.19
2							1.51	0.23	8.0	0.78	0.18	3.67	1.79	0.65	15.78	1.46	0.64	12.81
3													2.81	0.13	11.00	1.12	0.08	3.38

C adjacent to the vacancy. This impurity thus hosts three electrons. Due to the spin degree of freedom of the unpaired electron, the many-body ground state is two-fold degenerate forming a doublet state, whose wave functions can again be well approximated by a single Slater determinant in the band basis (see Table SX, Supporting Information). The ground state structure shows an out-of-plane distortion, mostly in the C position. Doublet–doublet excitations approximately promote the unpaired electron from the p_x orbital to delocalized p_z-like orbitals at the neighboring B ($D_0 \rightarrow D_1$ letting the C atom relax back to the plane), one of the electrons from the C p_z to the C p_x ($D_0 \rightarrow D_2$ with enhanced out-of-plane distortions) and the unpaired electron from the C p_x to C p_z ($D_0 \rightarrow D_3$ also letting the C position relaxing back to the plane). Here, the many-body energies are less influenced by modifications to the dielectric environment upon changing from bulk to monolayer hBN hosts. D_1, D_2, and D_3 change by about −0.03, −0.13, and −0.08 eV respectively, although, as before the effective density-density Coulomb matrix element is reduced by about $\Delta U^* \approx 0.15$ eV, while the single particle energies are affected by less than 5% when changing from the constrained-monolayer to the bulk hBN host. Thus only the D_2 transition approximately follows ΔU^*, while the other excitations are less affected. We attribute this different behavior to the difference in the nature of the excitations: D_1 and D_3 are single electron excitations, while D_2 takes place among three electrons and involves significant modifications to the impurity charge density. Under further relaxation toward the free-standing monolayer hBN, which enhances the out-of-plane distortion, the main difference is that the many-body states D_1 and D_2 become nearly degenerate. This is driven by modifications to the single-particle Kohn-Sham energies, while the screened Coulomb interactions are approximately the same (see monolayer to constrained-monolayer transition in Table SV, Supporting Information).

3.5.4. Huang-Rhys Factors

We now turn our focus to the Huang-Rhys factors S_{HR}. In Table 5 we summarize all ΔQ, $E_{FC,}$ and S_{HR} for both the free-standing monolayer and bulk hBN hosts. For both cases, we find that S_{HR} corresponding to the excited states in C_BC_N are considerably smaller than in C_BV_N and $C_BC_NV_N$ (note that our C_BC_N S_{HR} is in line with Refs. [29, 34]). Quantitatively this is driven by the decisive out-of-plane distortion of the $C_BV_N/C_BC_NV_N$ ground state, which is reduced in their excited states, yielding large ΔQ. This is related to the decisively modified impurity charge densities in $C_BV_N/C_BC_NV_N$ upon excitation. In the ground states, we find an in-plane charge density with p_x symmetry localized partially on carbon and partially on the nearest boron sites in presence of the N vacancy. Hartree terms (i.e., bare Coulomb repulsions) between these two partial densities destabilize the planar crystal structure, shifting the carbon up in z-direction in the ground state. Further full relaxation toward the free-standing monolayer limit enhances this out-of-plane distortion, which consequently increases S_{HR} via enhancing ΔQ. However, we note that in actual experiments these additional distortions are likely suppressed by the presence of a substrate or capping layer. In addition to ΔQ, there is also a slight but consistent trend of E_{FC} being less in bulk than in monolayer (C_BC_N is again the exception, though the change is negligible).

4. Discussion

In Section 2, we experimentally showed via PL measurements that the environment of carbon-based defects affected their properties, such as the energy of optical resonances and Huang-Rhys factors S_{HR}. In Section 3, we explored theoretically the possible mechanisms for these changes by comparing monolayer and bulk hBN hosts. In the following we summarize our findings, focusing mostly on defect complexes with technologically relevant intradefect transitions.

4.1. Mechanisms for Environmental Effects on Defect Properties

First, we consider differences in defect structure between monolayer and bulk hBN. These changes are relatively minor when the distortions related to the defect are purely in the hBN plane, as is the case for the single vacancies, single C impurities, and C_BC_N (see, e.g., **Table 5** and Supporting Information). For defects with ground-state out-of-plane corrugation (e.g., C_BV_N), the displacements are larger in monolayer than in bulk hBN hosts as there are no other hBN layers to constrain them (see Supporting Information). The effect of the increased distortions on the many-body energy differences and Frank-Condon relaxation energies is relatively modest. However, S_{HR} can be significantly larger in freestanding monolayer hBN hosts than in bulk ones for excitations accompanied by out-of-plane to in-plane geometry relaxations, which significantly increase ΔQ for the corresponding transitions.

We furthermore show that changing the hBN host environment mostly affects screened density–density Coulomb matrix

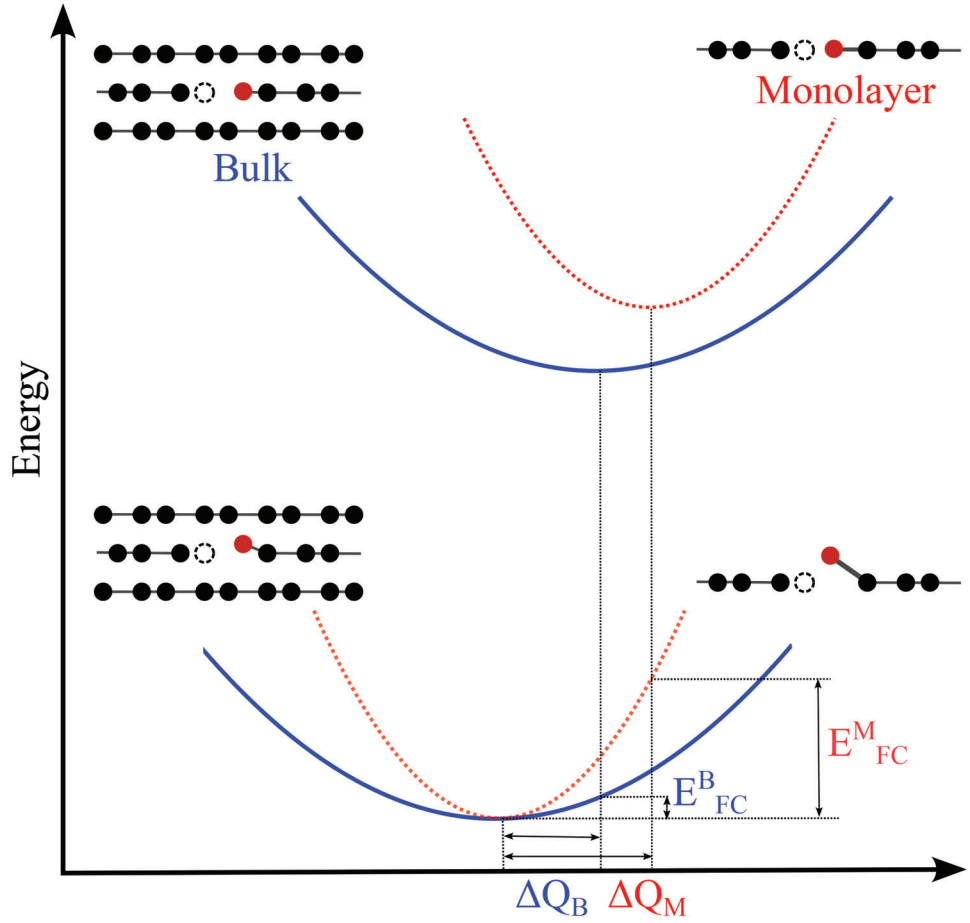

Figure 6. Configuration coordinate diagram for defect complexes embedded to bulk and monolayer sample.

elements within the impurity states, which can be reduced in the bulk by up to 1.3 eV, while single particle energies are modified by only up to 0.2 eV, and Hund's exchange Coulomb matrix elements barely change. Both the interorbital and intraorbital density–density interactions are reduced significantly in bulk hBN hosts by up to ≈ 50% compared to the monolayer case. Quantifying this change with an effective dielectric constant give $\epsilon_{\text{bulk}} \approx 3$ to 4, while $\epsilon_{\text{ML}} \approx 2$ to 2.5 depending on the defect. However, the extent to which these changes affect the intradefect many-body energies depends on how much the many-body levels depend on the interplay and compensation of the (partially various) density–density interactions and Hund's exchange parameter J. Overall, the resulting trend is that the energy separation of intradefect levels decreases in bulk hBN hosts compared to monolayer ones, which is, in general, most prominent in charge excitations.

4.2. Implications for Defect Identification

Our findings have significant implications for the identification of defects in hBN and 2DvdW layered hosts in general. First, we point out that renormalization of optical transitions from interactions and the correct treatment of spin symmetry is important for accurate comparison between experiment and theory, as is clear from comparing the KS single-particle states in Figure 5a–c with the many-body states (d–e). Here, this was achieved by our embedding approach, which can often also be achieved, e.g., via ΔSCF calculations utilizing hybrid functionals and possibly corrections for spin contamination[64] or higher-level multireference quantum chemistry approaches. A representative example of this observation is $C_B V_N$, wherein the single particle picture two transitions of about 2 eV are expected, while in the many-body picture the singlet–singlet transitions appear at energies above 3 eV, and triplet–triplet transition occur at about 1 eV (see Figure 5b,e).

Moreover, we have shown that intradefect transitions within 2DvdW hosts are controlled by additional degrees of freedom, i.e., the surrounding environment of the defects. In our optical measurements, this was tuned by the host-material thickness, while in theoretical calculations, we considered defects in bulk and monolayer hBN. The general trend of increasing intradefect energies and increasing S_{HR} in monolayer compared to bulk hosts are summarized in **Figure 6**: the host material can change both, ΔQ and E_{FC}. Thus, for experimental defect identifications within 2DvdW hosts, shifts in many-body energies and changes in S_{HR} should be taken into account across samples. On the other hand, such trends can be used to aid defect identification and characterization if a signal can

be correlated between samples of different thicknesses, or on different substrates.

In light of these results, we can reexamine the defects observed in the PL measurements. In the considered energy range, we observed four types of defects with varying emission energies and Huang-Rhys factors S_{HR}, which behave differently upon variation of the hBN film thickness. The defects A_2 and A_4 have PL resonances in the range of the doublet–doublet transitions related to V_N and V_B containing defects, respectively. However, S_{HR} for these defects is much larger than observed experimentally.[65] A_3 likely involves a defect similar to the carbon dimer, which might be coupled to neighboring vacancies, as it shows a relatively small S_{HR} and strong sensitivity of the PL resonance energy to the hBN film thickness. Defect A_1 is characterized by the largest S_{HR} and lowest emission energy (within our series). Assuming that A_1 is a simple defect, we could attribute it to the triplet–triplet transition within $C_B V_N$. However, it is also plausible that this defect does not belong to the defect space considered here. Interestingly, the investigated defects exhibit vanishing small Zeeman splitting, when the magnetic field is applied perpendicularly to the hBN plane (see Figure S5, Supporting Information). This observation may indicate that the optically active transitions are dominated by singlet–singlet transitions, however, the transitions between the parallel branches of the spin-split doublets and triples cannot be excluded.

Finally, we point out that we have not explicitly considered the effect of a substrate in this work. Depending on the substrate, the impact on the defect, properties may change significantly. On one hand, we would expect that the substrate could confine out-of-plane lattice distortions caused by the defect similar to the additional layer within bulk hBN hosts. On the other hand, the dielectric screening from certain substrates might be significantly larger compared to the moderate enhancement from monolayer to bulk hosts. Substrates with significant lattice contributions to the dielectric susceptibility may result in effective relative dielectric constants of 20 and above.[66,67]

4.3. Defects for Detecting Local Dielectric Susceptibility

We can use the sensitivity of defects in 2DvdW materials as probes of the local dielectric environment of, e.g., other surfaces, adsorbed molecules, or confined liquids.[68] An ideal defect for such applications should exhibit an optically accessible intra defect transition that has a strong dependence on the dielectric environment. Also, the defect should be characterized by a spectrally narrow optical signal providing good sensitivity and resolution for determining the properties of the dielectric environment. Thus, a small S_{HR} is desired. Finally, it would be ideal if the defect properties were relatively insensitive to other environmental stimuli such as external magnetic or electric fields.

Experimentally, defect A_3 appears as the best candidate for detecting the local dielectric constant. The PL emission resonance shifts by $\Delta E = 60.1$ meV between the 50 nm thick hBN film and ten-layer-thick hBN film. We can estimate the upper bound of the modification of the relative dielectric constant sensed by the defect within the two films based on our calculation to be $\Delta\epsilon < 2$. Therefore, we can conclude that our sensitivity toward the local dielectric constant is better than $\Delta\epsilon/\Delta E < 0.03$ meV^{-1}. The resolution is limited by the linewidth of the PL resonance δ, which also depends on the layer thickness. In the bulk form, the line exhibits its largest broadening, $\delta = 7.4$ meV, which corresponds to the change of the relative dielectric constant $\Delta\epsilon < 0.22$. In the monolayer form, $\delta = 1.5$ meV, which yields $\Delta\epsilon < 0.05$.

From our theoretical point of view, the singlet–singlet transition in C_BC_N is a promising candidate. Although it has rather high energy, its ZPL has been detected and identified previously.[20,22,29,58] Here, we have demonstrated that it is highly sensitive to the defect environment. Also, it has a Huang-Rhys factor that does not change with the dielectric environment, so its ZPL will remain sharp. Finally, it is a singlet–singlet transition, such that it likely will not be affected by stray magnetic fields. It may however, shift under the application of electric fields since the defect has a relatively low symmetry (point group C_{2v}).

Therefore, carbon defect centers in hBN can be used as sensitive detectors of local dielectric constants, addressing the need of measuring the environmental effects on a nanoscale.

5. Conclusion

Using a combination of experiment and theory, we have elucidated the effect of the dielectric environment and the local structure on defect properties in hBN. We show via PL measurements of few-layer and bulk-like samples, that carbon-based defects exhibit shifts in ZPL energies, as well as changes in phonon sidebands and ZPL lineshapes, which can be quantified via Huang-Rhys factors. Using first-principles theory and embedding methods applied to monolayer and bulk hBN, we show that the key effect of the environment arises from modifications in the effective local dielectric screening acting on the correlated impurities. This alters the inter- and intra-orbital impurity Coulomb interactions and plays a role in reducing optical emission energies for intradefect transitions in bulk versus mono/few-layer hBN hosts. These effects must be taken into account when performing defect identification via a comparison between experiment and theory. A plausible application of our findings is a detector for local dielectric constants, easily integrateble with solid, soft, and liquid matter systems in pristine and/or functionalized form.

6. Experimental Section

Crystal Growth: The pristine ultra-pure hBN crystals had been grown via the high-pressure temperature-gradient method. A part of the crystals from a single growth batch was annealed in a graphite furnace at a temperature of 2000°C for an hour.

Sample Fabrication: The hBN:C films were isolated through mechanical exfoliation of bulk crystals onto 300 nm thick Si/SiO_2 substrates. In the transfer process, the substrates were heated to 50°C to increase the yield of thin hBN:C flakes, which exhibit homogeneous and reproducible optical emission. The thickness of the films, typically ranging between a few layers to a few tens of nanometers, was determined by optical force microscopy.

For STM studies, hBN:C crystals were mechanically exfoliated onto 90 nm-thick Si/SiO_2 substrates. one up to three layer-thick films, identified via optical contrast and AFM techniques, were subsequently lifted with a PDMS/PC stamp and transferred onto a large graphite flake that was partially covered by a Cr/Au film, providing a conductive surface for the STM measurements. The samples were cleaned with DCM, ACE, and IPA, and finally annealed in an ultra-high vacuum in the STM chamber to remove any polymer residues from the transfer process.

Optical Characterization: The PL spectra were measured in a back-scattering geometry under continuous-wave 514 nm excitation. The sample was cooled down via exchange gas in a closed-loop cryostat or via cold finger in a cryostat cooled with liquid helium. The laser was focused on the surface of the sample to a spot of about 1 μm via an objective. The sample was positioned under the objective using *x-y-z* piezo-scanner system. The PL signal was resolved by a spectrometer and detected by a charge-coupled device camera. The second-order photon correlations were measured in the Hanbury-Brown and Twiss configuration with avalanche photodiodes acting as photon detectors.

Scanning Tunneling Microscopy: The scanning tunneling microscopy was done in a low-temperature Createc system with base pressure below 10^{-10} mbar. In these samples, the tunnelling occurred between the tungsten tip and graphite substrate through a three-layer-thick carbon-doped hBN barrier. The *dI/dV* tunnelling spectra were measured at a modulated voltage between 3 and 10 meV at the frequency of 700–900 Hz. The tip was calibrated for spectroscopy against the surface state of gold in 111 orientation.

Theoretical Methods: Density functional (DFT) electronic structure calculations were performed within the Vienna *ab initio* simulation package (VASP)[69,70] utilizing the projector-augmented wave (PAW)[71] formalism with PBE generalized-gradient approximation (GGA)[72] of exchange-correlation functional. For details on of the mapping to the minimal models and their solutions see Supporting Information.

Supporting Information

Supporting Information is available from the Wiley Online Library or from the author.

Acknowledgements

This project was supported by the Ministry of Education (Singapore) through the Research Centre of Excellence program (grant EDUN C-33-18-279-V12, I-FIM), AcRF Tier 3 (MOE2018-T3-1-005). This material was based upon work supported by the Air Force Office of Scientific Research and the Office of Naval Research Global under award number FA8655-21-1-7026. This research was supported by the Ministry of Education, Singapore, under its Academic Research Fund Tier 2 (MOE-T2EP50122-0012). J. Lu acknowledges the support from Agency for Science, Technology and Research (A*STAR) under its AME IRG Grant (Project no. M21K2c0113). K.W. and T.T. acknowledge support from JSPS KAKENHI (Grant Numbers 19H05790, 20H00354, and 21H05233). P.H. acknowledges the supports of the National Key Research and Development Program (2021YFB3802400) and the National Natural Science Foundation (52161037) of China. M.P acknowledges the support from EU Graphene Flagship and FNP-Poland (IRA - MAB/2018/9 grant, SG 0P program of the EU). C.R.F acknowledges the European Union's Horizon 2020 research and innovation programme under the Marie Skłodowska-Curie grant agreement N° 895369. The computational work for this article was performed on resources at the National Supercomputing Centre, Singapore. C.E.D. acknowledges support from the National Science Foundation under Grant no. DMR-2237674. D.I.B. was supported by the European Research Council (ERC) under the European Union's Horizon 2020 research and innovation programme, grant agreement 854843-FASTCORR.

Conflict of Interest

The authors declare no conflict of interest.

Data Availability Statement

The data that support the findings of this study are available from the corresponding author upon reasonable request.

Keywords

carbon centers in hexagonal boron nitride, dielectric environment, embedded impurities, screening effects to impurities

Received: January 5, 2023
Revised: June 1, 2023
Published online: June 17, 2023

[1] J. R. Weber, W. F. Koehl, J. B. Varley, A. Janotti, B. B. Buckley, C. G. Van de Walle, D. D. Awschalom, *P. Natl. Acad. Sci.* **2010**, *107*, 8513.
[2] B. E. Kane, *Nature* **1998**, *393*, 133.
[3] J. J. Pla, K. Y. Tan, J. P. Dehollain, W. H. Lim, J. J. L. Morton, D. N. Jamieson, A. S. Dzurak, A. Morello, *Nature* **2012**, *489*, 541.
[4] Y. Wu, Y. Wang, X. Qin, X. Rong, J. Du, *npj Quantum Inf.* **2019**, *5*, 9.
[5] I. Aharonovich, S. Castelletto, D. A. Simpson, C.-H. Su, A. D. Greentree, S. Prawer, *Rep. Prog. Phys.* **2011**, *74*, 076501.
[6] I. Aharonovich, A. D. Greentree, S. Prawer, *Nat. Photonics* **2011**, *5*, 397.
[7] R. Schirhagl, K. Chang, M. Loretz, C. L. Degen, *Annu. Rev. Phys. Chem.* **2014**, *65*, 83.
[8] D. Lee, D. Gohlke, A. Benjamin, J. A. Gupta, *J. Phys.: Condens. Matter* **2015**, *27*, 154202.
[9] D. Lee, J. A. Gupta, *Nanophotonics* **2019**, *8*, 2033.
[10] Y. Kubota, K. Watanabe, O. Tsuda, T. Taniguchi, *Science* **2007**, *317*, 932.
[11] G. Cassabois, P. Valvin, B. Gil, *Nat. Photonics* **2016**, *10*, 262.
[12] H. Wang, Y. Zhao, Y. Xie, X. Ma, X. Zhang, *J. Semicond.* **2017**, *38*, 031003.
[13] T. T. Tran, K. Bray, M. J. Ford, M. Toth, I. Aharonovich, *Nat. Nanotechnol.* **2016**, *11*, 37.
[14] T. T. Tran, C. Elbadawi, D. Totonjian, C. J. Lobo, G. Grosso, H. Moon, D. R. Englund, M. J. Ford, I. Aharonovich, M. Toth, *ACS Nano* **2016**, *10*, 7331.
[15] M. Koperski, K. Nogajewski, M. Potemski, *Opt. Commun.* **2018**, *411*, 158.
[16] M. E. Turiansky, A. Alkauskas, L. C. Bassett, C. G. Van de Walle, *Phys. Rev. Lett.* **2019**, *123*, 127401.
[17] A. L. Exarhos, D. A. Hopper, R. N. Patel, M. W. Doherty, L. C. Bassett, *Nat. Commun.* **2019**, *10*, 1.
[18] V. Ivády, G. Barcza, G. Thiering, S. Li, H. Hamdi, J.-P. Chou, Ö. Legeza, A. Gali, *npj Comput. Mater.* **2020**, *6*, 41.
[19] N.-J. Guo, W. Liu, Z.-P. Li, Y.-Z. Yang, S. Yu, Y. Meng, Z.-A. Wang, X.-D. Zeng, F.-F. Yan, Q. Li, J.-F. Wang, J.-S. Xu, Y.-T. Wang, J.-S. Tang, C.-F. Li, G.-C. Guo, *ACS Omega* **2022**, *7*, 1733.
[20] L. Museur, E. Feldbach, A. Kanaev, *Phys. Rev. B* **2008**, *78*, 155204.
[21] O. L. Krivanek, M. F. Chisholm, V. Nicolosi, T. J. Pennycook, G. J. Corbin, N. Dellby, M. F. Murfitt, C. S. Own, Z. S. Szilagyi, M. P. Oxley, S. T. Pantelides, S. J. Pennycook, *Nature* **2010**, *464*, 571.
[22] X. Z. Du, J. Li, J. Y. Lin, H. X. Jiang, *Appl. Phys. Lett* **2015**, *106*, 021110.
[23] M. R. Uddin, J. Li, J. Y. Lin, H. X. Jiang, *Appl. Phys. Lett.* **2017**, *110*, 182107.
[24] M. Koperski, D. Vaclavkova, K. Watanabe, T. Taniguchi, K. S. Novoselov, M. Potemski, *PNAS* **2020**, *117*, 13214.
[25] N. Mendelson, D. Chugh, J. R. Reimers, T. S. Cheng, A. Gottscholl, H. Long, C. J. Mellor, A. Zettl, V. Dyakonov, P. H. Beton, S. V. Novikov, C. Jagadish, H. H. Tan, M. J. Ford, M. Toth, C. Bradac, I. Aharonovich, *Nat. Mater.* **2021**, *20*, 321.
[26] C. Attaccalite, M. Bockstedte, A. Marini, A. Rubio, L. Wirtz, *Phys. Rev. B* **2011**, *83*, 144115.
[27] B. Huang, H. Lee, *Phys. Rev. B* **2012**, *86*, 245406.

[28] J. R. Reimers, A. Sajid, R. Kobayashi, M. J. Ford, *J. Chem. Theory Comput.* **2018**, *14*, 1602.
[29] M. Mackoit-Sinkevičienė, M. Maciaszek, C. G. Van de Walle, A. Alkauskas, *Appl. Phys. Lett.* **2019**, *115*, 212101.
[30] A. Sajid, K. S. Thygesen, *2D Mater.* **2020**, *7*, 031007.
[31] M. Chojecki, E. Lewandowska, T. Korona, *J Mol Model* **2020**, *26*, 216.
[32] P. Auburger, A. Gali, *Phys. Rev. B* **2021**, *104*, 075410.
[33] L. Muechler, D. I. Badrtdinov, A. Hampel, J. Cano, M. Rösner, C. E. Dreyer, *Phys. Rev. B* **2022**, *105*, 235104.
[34] M. Winter, M. H. E. Bousquet, D. Jacquemin, I. Duchemin, X. Blase, *Phys. Rev. Mater.* **2021**, *5*, 095201.
[35] D. S. Wang, C. J. Ciccarino, J. Flick, P. Narang, *ACS nano* **2021**, *15*, 5240.
[36] M. Maciaszek, L. Razinkovas, A. Alkauskas, *Phys. Rev. Mater.* **2022**, *6*, 014005.
[37] P. Huang, M. Grzeszczyk, K. Vaklinova, K. Watanabe, T. Taniguchi, K. S. Novoselov, M. Koperski, *Phys. Rev. B* **2022**, *106*, 014107.
[38] N. R. Jungwirth, B. Calderon, Y. Ji, M. G. Spencer, M. E. Flatté, G. D. Fuchs, *Nano Lett.* **2016**, *16*, 6052.
[39] A. Raja, A. Chaves, J. Yu, G. Arefe, H. M. Hill, A. F. Rigosi, T. C. Berkelbach, P. Nagler, C. Schüller, T. Korn, C. Nuckolls, J. Hone, L. E. Brus, T. F. Heinz, D. R. Reichman, A. Chernikov, *Nat. Commun.* **2017**, *8*, 15251.
[40] K. Andersen, S. Latini, K. S. Thygesen, *Nano Lett.* **2015**, *15*, 4616.
[41] A. Steinhoff, M. Florian, M. Rösner, G. Schönhoff, T. O. Wehling, F. Jahnke, *Nature Communications* **2017**, *8*, 1166.
[42] D. Soriano, A. N. Rudenko, M. I. Katsnelson, M. Rösner, *npj Comput. Mater.* **2021**, *7*, 1.
[43] A. M. Stoneham, *Theory of Defects in Solids: Electronic Structure of Defects in Insulators and Semiconductors*, Oxford University Press, Oxford, UK **2001**.
[44] M. Koperski, K. Pakuła, K. Nogajewski, A. K. Dąbrowska, M. Tokarczyk, T. Pelini, J. Binder, T. Fąs, J. Suffczyński, R. Stępniewski, A. Wysmołek, M. Potemski, *Scientific Reports* **2021**, *11*, 15506.
[45] T. T. Tran, C. Elbadawi, D. Totonjian, C. J. Lobo, G. Grosso, H. Moon, D. R. Englund, M. J. Ford, I. Aharonovich, M. Toth, *ACS Nano* **2016**, *10*, 7331.
[46] A. Alkauskas, B. B. Buckley, D. D. Awschalom, C. G. Van De Walle, *New J. Phys.* **2014**, *16*, 073026.
[47] L. Razinkovas, M. W. Doherty, N. B. Manson, C. G. Van de Walle, A. Alkauskas, *Phys. Rev. B* **2021**, *104*, 045303.
[48] A. Alkauskas, M. D. McCluskey, C. G. Van de Walle, *J. Appl. Phys.* **2016**, *119*, 181101.
[49] A. Alkauskas, J. L. Lyons, D. Steiauf, C. G. Van de Walle, *Phys. Rev. Lett.* **2012**, *109*, 267401.
[50] A. Alkauskas, C. E. Dreyer, J. L. Lyons, C. G. Van de Walle, *Phys. Rev. B* **2016**, *93*, 201304(R).
[51] F. Aryasetiawan, M. Imada, A. Georges, G. Kotliar, S. Biermann, A. I. Lichtenstein, *Phys. Rev. B* **2004**, *70*, 195104.
[52] A. Laturia, M. L. Van de Put, W. G. Vandenberghe, *npj 2D Mater. Appl.* **2018**, *2*, 6.
[53] S. F. Chichibu, Y. Ishikawa, H. Kominami, K. Hara, *J. Appl. Phys.* **2018**, *123*, 6, 065104.
[54] A. K. Dabrowska, M. Tokarczyk, G. Kowalski, J. Binder, R. Bozek, J. Borysiuk, R. Stepniewski, A. Wysmolek, *2D Mater.* **2020**, *8*, 015017.
[55] C.-Y. Moon, K.-S. Hong, Y.-S. Kim, *Advances in Condensed Matter Physics* **2022**, *2022*, e1036942.
[56] M. Rösner, E. Şaşioğlu, C. Friedrich, S. Blügel, T. O. Wehling, *Phys. Rev. B* **2015**, *92*, 085102.
[57] A. Sajid, M. J. Ford, J. R. Reimers, *Rep. Prog. Phys.* **2020**, *83*, 044501.
[58] K. Era, F. Minami, T. Kuzuba, *J. Lumin.* **1981**, *24-25*, 71.
[59] C. Linderälv, W. Wieczorek, P. Erhart, *Phys. Rev. B* **2021**, *103*, 115421.
[60] C. Jara, T. Rauch, S. Botti, M. A. L. Marques, A. Norambuena, R. Coto, J. E. Castellanos-Águila, J. R. Maze, F. Munoz, *J. Phys. Chem. A* **2021**, *125*, 1325.
[61] O. N. Ocampo, Ph.D. thesis. Université Paris Sacla, Paris **2017**.
[62] M. Schüler, M. Rösner, T. O. Wehling, A. I. Lichtenstein, M. I. Katsnelson, *Phys. Rev. Lett.* **2013**, *111*, 036601.
[63] D. J. Carrascal, J. Ferrer, J. C. Smith, K. Burke, *J. Phys.: Condens. Matter* **2015**, *27*, 393001.
[64] U. von Barth, *Phys. Rev. A* **1979**, *20*, 1693.
[65] S. Li, A. Gali, *Frontiers Quant. Sci. Tech.* **2022**, *1*,1007756. .
[66] K. A. Müller, H. Burkard, *Phys. Rev. B* **1979**, *19*, 3593.
[67] J. Robertson, *Eur. Phys. J. Appl. Phys.* **2004**, *28*, 265.
[68] L. Fumagalli, A. Esfandiar, R. Fabregas, S. Hu, P. Ares, A. Janardanan, Q. Yang, B. Radha, T. Taniguchi, K. Watanabe, G. Gomila, K. S. Novoselov, A. K. Geim, *Science* **2018**, *360*, 1339.
[69] G. Kresse, J. Hafner, *Phys. Rev. B* **1993**, *47*, 558.
[70] G. Kresse, J. Furthmüller, *Phys. Rev. B* **1996**, *54*, 11169.
[71] P. E. Blöchl, *Phys. Rev. B* **2000**, *62*, 6158.
[72] J. P. Perdew, K. Burke, M. Ernzerhof, *Phys. Rev. Lett.* **1996**, *77*, 3865.